

Progress in Computational Fluid Dynamics, An International Journal

ISSN online: 1741-5233 - ISSN print: 1468-4349
<https://www.inderscience.com/pcfd>

Effect of aspect ratio of semitransparent window on interaction of the collimated beam with natural convection: part 1

G. Chanakya, Pradeep Kumar

DOI: [10.1504/PCFD.2021.10045438](https://doi.org/10.1504/PCFD.2021.10045438)

Article History:

Received:	08 April 2021
Last revised:	02 December 2021
Accepted:	02 December 2021
Published online:	02 February 2023

Effect of aspect ratio of semitransparent window on interaction of the collimated beam with natural convection: part 1

G. Chanakya and Pradeep Kumar*

Numerical Experiment Laboratory
(Radiation & Fluid Flow Physics),
School of Engineering,
Indian Institute of Technology Mandi,
Mandi, Himachal Pradesh, 175075, India
Email: chandrasekhara_pratap@students.iitmandi.ac.in
Email: pradeepkumar@iitmandi.ac.in
*Corresponding author

Abstract: The effect of the semitransparent window's aspect ratio, i.e., the height ratio (h_r) and window width ratio (w_r) and Planck numbers on the interaction of the collimated beam with natural convection has been investigated numerically. The cavity is convectively heated from the bottom, and a semitransparent window is created on the left wall, and a collimated beam is irradiated on the window at an azimuthal angle (ϕ) of 135° . The dynamics of two vortices inside the cavity change considerably by combination of window's aspect ratio and Planck number (Pl) of the medium. The thermal plume flickers depending on the situation of the dynamics of two vortices inside the cavity. The localised heating of the fluid happens mostly for the large height ratio of the semitransparent window. The conduction, radiation, and total Nusselt numbers are also greatly affected by the aspect ratio and Planck number of the medium.

Keywords: semitransparent wall; natural convection; collimated beam irradiation; symmetrical cooling; aspect ratio.

Reference to this paper should be made as follows: Chanakya, G. and Kumar, P. (2023) 'Effect of aspect ratio of semitransparent window on interaction of the collimated beam with natural convection: part 1', *Progress in Computational Fluid Dynamics*, Vol. 23, No. 1, pp.34–51.

Biographical notes: G. Chanakya is currently a PhD student in the School of Engineering at the Indian Institute of Technology Mandi, Mandi, Himachal Pradesh, India. He obtained his Master's degree from the National Institute of Technology Silchar, Assam, India. He is currently working on numerical modelling of diffuse and collimated beam radiation and its interaction with natural convection.

Pradeep Kumar received his PhD from the Indian Institute of Technology Kanpur, Kanpur in 2009. Afterwards, he worked with ANSYS Fluent for more than six years. Currently, he is working as an Assistant Professor in the School of Engineering at the Indian Institute of Technology Mandi, Mandi, Himachal Pradesh, India. His research activities include numerical modelling of the interaction of radiation with fluid flow using OpenFOAM. He is also involved in the development of a spectral radiative model using HITEMP database for engineering applications, like, combustion, Plume radiation, solar cavity receivers, etc.

1 Introduction

A collimated beam of electromagnetic radiation is a typical beam of light which has low beam divergence as it propagates in a medium. Collimated beams are useful in many engineering applications like, fibre optics, additive manufacturing techniques, collimated beam induced natural convection, solar energy applications, etc. The study of greenhouse gas effect, heating, ventilation, and air conditioning systems (HVAC), shallow water dynamic,

marine life, etc. involve collimated beam radiation. In fact, the glass windows (semitransparent wall) and their aspect ratios plays a vital role in the heat transfer in a room and greatly affects the performance of HVAC systems. In such scenarios, the analysis of natural convection induced by collimated beam radiation is a subject of a great interest to the researchers. Though, the practical applications involve complex geometries, however, physics can be very well understood by analysing the phenomena in a simple geometry. Comprehensive reviews of the natural convection

in practical geometries for engineering applications were compiled by Das et al. (2017) and Rahimi et al. (2019).

The characteristics of buoyancy flow change with the aspect ratio of the enclosure and its orientation as well as with the boundary conditions. Natural convection in square/rectangular enclosures heated from the bottom and cooled from the top (Hasnaoui et al., 1992) or sides (Ganzarolli and Milanez, 1995; Aydin and Yang, 2000; Calcagni et al., 2005) revealed that the flow field and temperatures were sensitive to the aspect ratio and position of the heat source. Furthermore, Yigit et al. (2015) also reported that the aspect ratio of the geometry had a significant impact on the formation of convective vortices.

A collimated beam is illuminated on one side of the test case to study the effect of radiative heating on the natural convection by Webb and Viskanta (1987) and they showed the formation of a thin hydrodynamic boundary layer at the vertical wall, and the flow structure had lost its centrosymmetry nature. Further, Karatas and Derbentli (2018) experimental work revealed that the change in the aspect ratio had greatly affected the heat transfer inside the enclosure. Further, they proposed the heat transfer correlations as the function of Rayleigh number, Prandtl number and the aspect ratio. Though the inclusion of radiation has an impact on heat transfer characteristics, the radiative transfer equation (RTE) is computationally expensive to solve due to its spectral and directional dependence. An assumption of the grey medium, on the other hand, can substantially simplify this difficulty. Various radiation models, such as Monte Carlo method (MCM), discrete transfer technique (DTM), zonal methods, discrete ordinate method (DOM) (Chai et al., 1993), and finite volume discrete ordinate method (FVDOM) (Raithby and Chui, 1990; Chui and Raithby, 1993), have been widely employed in situations involving radiative heat transport. Sun et al. (2017) investigated the performance of various RTE techniques such as P1, SP3, P3, DOM, and FVDOM. Their results revealed that the P1 method took minimal time but suffered inaccuracy for the low optical thickness medium than any other methods. Whereas, FVDOM on the other hand, was more accurate than DOM but took more computational time.

Furthermore, natural convection coupled with radiation in an emitting, absorbing, and scattering medium was investigated for various aspect ratios (Fu et al., 2015) with various parameters such as Planck numbers, wall emissivity, scattering albedo, and extinction coefficient (Mondal and Mishra, 2008), and these parameters significantly influenced the heat transfer characteristics inside the cavity. The numerical works of Mezrhab et al. (2006), Sun et al. (2011), Kumar and Eswaran (2013) and Parmananda et al. (2017) showed that the radiation exchange homogenised the temperature field inside the cavity.

The above works have mainly considered either pure natural convection, or coupled diffuse radiation and natural convection, however, only a few works considering the collimated beam radiation is reported in the literature, like, discrete transfer method (DTM) (Abdallah and Le Dez,

2000) was used to solve RTE in participating media and derived the exact radiative flux (Krishna and Mishra, 2006) field expression for the linearly varying refractive index. The thermal damage in the proximity of the laser source was evaluated by using the transient radiation transfer equation by Verma et al. (2016). Further, the initiation of phototactic bioconvection for an algal has been investigated by Vincent and Hill (1996), Kong and Vigil (2014), Panda et al. (2016), Panda (2020) and Bees (2020). Recently, the effect of diffuse and collimated beam radiation on the natural convection on symmetrical cooling from the side has been studied by Chanakya and Kumar (2021a). They further investigated the effect of the thermal adiabatic boundary conditions on the semitransparent wall of the cavity (Chanakya and Kumar, 2021b).

It is evident from the aforementioned literature that under various conditions, aspect ratio affects the flow and temperature distributions greatly inside the system. The present work investigates the effect of an aspect ratio of semitransparent window through which collimated beam travels inside the cavity, on the natural convection. The medium inside the cavity is absorbing/emitting without scattering. This is the first work of its kind to the best of the authors' knowledge at present.

This paper is outlined as follows: problem description is defined in Section 2, followed by mathematical modelling and numerical scheme in Section 3. Non-dimensional parameters are provided in Section 4. Verification and independent tests for grids are explained in Sections 5 and 6, respectively. Section 7 elaborates results and discussion for the variation of Planck numbers and aspect ratios. Finally, conclusions of this numerical study are provided in Section 8.

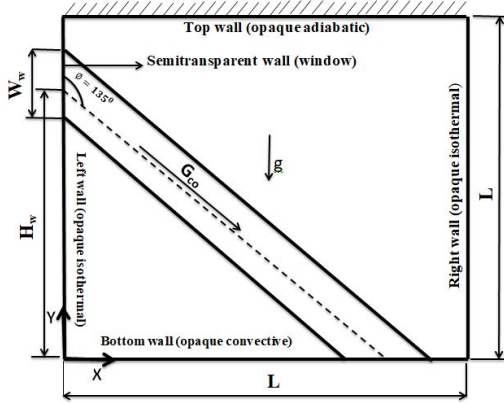
2 Problem description

Consider the buoyancy driven flow of Newtonian fluid within the square enclosure due to heating of bottom wall by convective heating with a free stream temperature of 305 K and a heat transfer coefficient of 50 W/m²K as depicted in Figure 1. The top wall is considered adiabatic and the right and left walls are isothermal conditions at a temperature of 296 K. The Euclidean coordinate axes are along the bottom and left vertical walls of the enclosure and origin is at the junction of these two walls. The acceleration due to gravity acts vertically in a downward direction (negative direction). All walls of the enclosure are treated as opaque with an emissivity of 0.9 for the outgoing radiation. The four semitransparent window aspect ratio combinations, height ratio ($h_r = H_w/L$) and window width ratio ($w_r = W_w/L$), have been considered as below:

- case A: $h_r = 0.8$ and $w_r = 0.2$
- case B: $h_r = 0.8$ and $w_r = 0.4$
- case C: $h_r = 0.4$ and $w_r = 0.2$
- case D: $h_r = 0.4$ and $w_r = 0.4$.

In all the above cases (i.e., A, B, C and D), a collimated beam of irradiation value $1,000 \text{ W/m}^2$ is applied on the semitransparent window at an azimuthal angle 135° . The semitransparent window is also at temperature 296 K (isothermal boundary). The simulations are carried out for the constant flow parameter ($Ra = 10^5$) and fluid parameter ($Pr = 0.71$), thermal parameter ($N = 1.5$) and various semitransparent window's aspect ratios and Planck numbers ($Pl = 0, 1, 10$ and 50).

Figure 1 The schematic diagram of the present problem where a collimated beam is incident on semitransparent window at an azimuthal angle 135°



3 Mathematical formulation and numerical procedures

The following assumptions have been considered for the mathematical modelling of the above problem:

- 1 flow is two-dimensional, steady, laminar and incompressible
- 2 flow is driven by buoyancy force which is modelled by Boussinesq approximation
- 3 the thermophysical properties of the fluid are constant
- 4 the fluid medium absorbs/emits but does not scatter the radiation energy
- 5 the transmissivity of the semitransparent window is one for the incoming radiation and zero for the outgoing radiation.

Based on the above assumptions, the governing equations (Kumar and Eswaran, 2013; Chanakya and Kumar, 2021a, 2021b) in the Cartesian coordinate system are given as:

$$\frac{\partial u_i}{\partial x_i} = 0, \quad (1)$$

$$\frac{\partial u_i u_j}{\partial x_j} = -\frac{1}{\rho} \frac{\partial p}{\partial x_i} + \nu \frac{\partial^2 u_i}{\partial x_j \partial x_j} + g \beta_T (T - T_c) \delta_{i2}, \quad (2)$$

$$\frac{\partial u_j T}{\partial x_j} = \frac{k}{\rho C_p} \frac{\partial^2 T}{\partial x_j \partial x_j} - \frac{1}{\rho C_p} \frac{\partial q_R}{\partial x_i}, \quad (3)$$

where u , p , ρ , β_T , g , c_p and κ are velocity, pressure, density, thermal expansion coefficient, gravity, specific heat capacity at constant pressure and thermal conductivity of fluid, respectively. i, j are tensor indices which vary from 1 to 2 in Cartesian coordinates system. The δ_{i2} is Kronecker delta defined as

$$\delta_{i2} = \begin{cases} 0, & \text{if } i \neq 2, \\ 1, & \text{if } i = 2. \end{cases}$$

- Flow boundary condition:

no slip: $u_i = 0$.

- Thermal boundary conditions:

1 left wall at $X = 0$: $T = 296 \text{ K}$

2 right wall at $X = 1$: $T = 296 \text{ K}$

3 bottom wall at $Y = 0$:

$$q_{conv} = h_{free}(T_{free} - T_w)$$

4 top wall at $Y = 1$: $q_c + q_r = 0$

where $q_c = -k \frac{\partial T}{\partial n}$ and $q_r = \int_{4\pi} I(\mathbf{r}_w, \mathbf{s})(\hat{\mathbf{n}} \cdot \mathbf{s}) d\Omega$.

The $\frac{\partial q_{R_i}}{\partial x_i}$ in equation (3) is the divergence of radiative flux which is calculated as

$$\frac{\partial q_{R_i}}{\partial x_i} = \kappa_a (4\pi I_b - G), \quad (4)$$

where κ_a , I_b and G are absorption coefficient, black body intensity and irradiation which is evaluated by integrating the radiative intensity (I) in all directions, i.e.,

$$G = \int_{4\pi} I d\Omega, \quad (5)$$

The radiative intensity field inside the cavity can be obtained by solving the following radiative transfer equation

$$\frac{\partial I(\mathbf{r}, \mathbf{s})}{\partial s} = \kappa_a (I_b(\mathbf{r}, \mathbf{s}) - I(\mathbf{r}, \mathbf{s})), \quad (6)$$

where \mathbf{r} and \mathbf{s} are position and direction vectors, respectively, and s is path length in the beam direction.

The Navier-stokes and energy equations are subjected to the following boundary conditions.

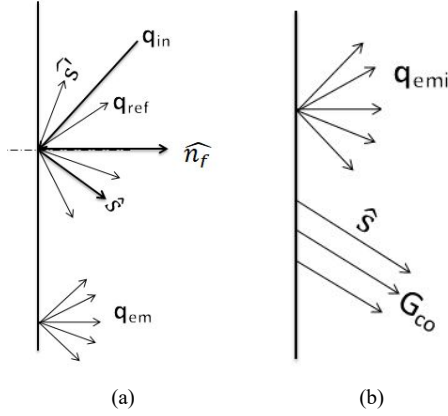
The radiative transfer equation (6) is subjected to grey diffusely emitting and reflecting wall [shown in Figure 2(a)] (Modest, 2013) as below,

$$I(\mathbf{r}_w, \mathbf{s}) = \epsilon_w I_b(\mathbf{r}_w) + \frac{1 - \epsilon_w}{\pi} \int_{\hat{\mathbf{n}} \cdot \mathbf{s} > 0} I(\mathbf{r}_w, \mathbf{s}') |\hat{\mathbf{n}} \cdot \mathbf{s}'| d\Omega, \quad (7)$$

for $\hat{\mathbf{n}} \cdot \mathbf{s} < 0$

where $\hat{\mathbf{n}}$ is the unit normal surface area and the ϵ is emissivity of the walls and is considered as 0.9 for present study for all walls.

Figure 2 The pictorial representation of, (a) diffuse reflection of an incident ray and diffuse emission due to wall temperature (b) diffuse emission and collimated transmission from a semitransparent wall



The semitransparent window is subjected to diffuse emission and collimated irradiation as shown in Figure 2(b) with an collimated irradiation (G_{co}) of value $1,000 \text{ W/m}^2$. The boundary condition for RTE on the semitransparent window is

$$I(\mathbf{r}_w, \mathbf{s}) = I_{co}(\mathbf{r}_w, \mathbf{s})\delta(\phi - 135^\circ) + \epsilon_w I_b(\mathbf{r}_w) + \frac{1 - \epsilon_w}{\pi} \int_{\hat{\mathbf{n}} \cdot \mathbf{s} > 0} I(\mathbf{r}_w, \mathbf{s}') |\hat{\mathbf{n}} \cdot \mathbf{s}'| d\Omega' \quad (8)$$

for $\hat{\mathbf{n}} \cdot \mathbf{s} < 0$

where $\delta(\phi - 135^\circ)$ is Dirac-delta function, and defined as

$$\delta(\phi - 135^\circ) = \begin{cases} 1, & \text{if } \phi = 135^\circ, \\ 0, & \text{if } \phi \neq 135^\circ. \end{cases}$$

In the current work, the solid angle ($d\Omega$) of discretised angular space [Figure 3(b)] is considered as the collimated beam width. The intensity of collimated beam irradiation I_{co} is obtained from the below equation,

$$I_{co} = \frac{G_{co}}{d\Omega}, \quad (9)$$

The FVM integrates an partial differential equation over a control volume [Figure 3(a)] along with boundary conditions to convert the partial differential equation into a set of algebraic equations of the form

$$a_p \phi_p = \sum_{nb} a_{nb} \phi_{nb} + S \quad (10)$$

where ϕ_p is a scalar, a_p is a central coefficient, a_{nb} a coefficients of neighbouring cells and S is the source term.

In the present work, the OpenFOAM application buoyantBoussinesqSimpleFoam (bBSF) (OpenFOAM, 2017) is employed, it has fluid flow and heat transfer libraries including library for FVDOM. This application uses semi-implicit method for pressure linked equations (SIMPLE) (Patankar, 2018) algorithm for the momentum equation with preconditioner diagonal incomplete LU

decomposition (DILU) (Chanakya and Kumar, 2021b; Moukalled et al., 2016). A linear-upwind scheme is used for the convection term, which is second order accurate and is given mathematically as

$$\phi_f = \begin{cases} \phi_p + \nabla \phi_p \cdot \vec{r}, & \text{if } f_\phi > 0, \\ \phi_{nb} + \nabla \phi_{nb} \cdot \vec{r}, & \text{if } f_\phi < 0. \end{cases} \quad (11)$$

where f_ϕ is the flux of the scalar ϕ on a face [Figure 3(a)], and p, nb indicate present and neighbouring cells and f indicates face value of a scalar. The pressure equation is solved using geometric algebraic multi-grid (GAMG) with smoother-diagonal incomplete-Cholesky Gauss-Seidel (DICGaussSeidel).

Moreover, the FVDOM is also employed to discretise the RTE as it provides the versatility in the selection of directions. The RTE [equation (6)] represents the transfer of radiative energy in single direction and in order to obtain total radiation energy from all directions in a single cell, equation (6) equation needs to be integrated over each control volume [Figure 3(a)] and control angle [Figure 3(b)] which yields the discretised radiative transfer equation. For the grey gas without any scattering assumption, it entails

$$\int_{d\Omega^i} \int_{dV} \nabla \cdot (\mathbf{s} I^i) dV d\Omega = \int_{d\Omega^i} \int_{dV} k [I_b(\mathbf{r}) - I^i(\mathbf{r}, \mathbf{s})] dV d\Omega \quad (12)$$

where I^i is the intensity in direction \mathbf{s} (total angular directions is discretised into many control angles, $d\Omega^i$, i represents the index for the control angles). By applying Gauss's divergence theorem to the above equation we get,

$$\int_{d\Omega^i} \int_{dA} I^i(\mathbf{s} \cdot \mathbf{n}) dA d\Omega = \int_{d\Omega^i} \int_{dV} \kappa (I_b - I^i) dV d\Omega \quad (13)$$

where \mathbf{n} is the unit normal vector of control volume face. The surface integral can be approximated by the sum over the control volume faces, assuming that the radiation intensity is constant on each of the control volume faces. The intensity is also expected to be constant inside the control volume and throughout the finite solid angle $d\Omega$. Thus, equation (13) can be expressed as

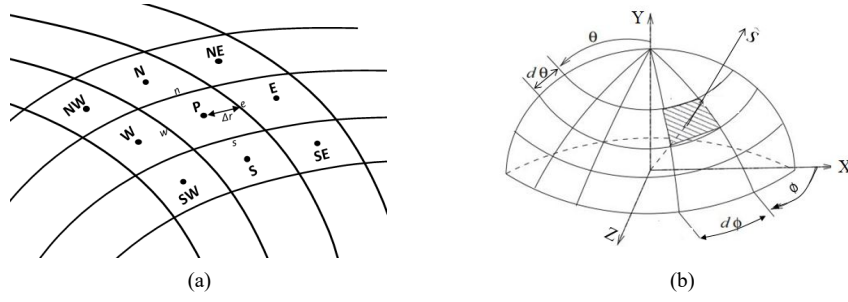
$$\sum_f I_f^i A_f D_f^i = \kappa (-I_p^i + I_{b,c}) dV d\Omega^i \quad (14)$$

where the face index f represents the east (E), west (W), north (N), and south (S) faces and P indicates the cell centroid. The directional weight D_f^i can be expressed as,

$$D_f^i = \int_{d\Omega^i} (\mathbf{s}^i \cdot \mathbf{n}_f) d\Omega \quad (15)$$

and \mathbf{n}_f is the outward surface normal to a face f , \mathbf{s}^i is the direction of the pencil of a ray and $d\Omega$ is the solid angle corresponding to the direction i .

Figure 3 The pictorial representation of (a) cell arrangement for finite volume method for partial differential equations and (b) angular discretisation for the radiative transfer equation



The spherical coordinate system is used to discretise the angular space, Where, a direction is described by polar (θ) and azimuthal (ϕ) angles as shown in Figure 3(b). The direction of a pencil of rays (\mathbf{s}) and the solid angle $d\Omega$ are expressed as below

$$\mathbf{s} = \sin \theta \sin \phi \hat{i} + \sin \theta \cos \phi \hat{j} + \cos \theta \hat{k} \quad (16)$$

and a solid angle is described in polar and azimuthal directions (θ, ϕ) as

$$d\Omega = 2 \sin \theta \sin \left(\frac{d\theta}{2} \right) d\phi \quad (17)$$

Thus, directional weight D_f^i is calculated as below,

$$\begin{aligned} D_f^i &= \sin \phi \sin \left(\frac{d\phi}{2} \right) \left[d\theta - \cos(2\theta) \sin(d\theta) \right] \hat{i} \\ &+ \cos \phi \sin \left(\frac{d\phi}{2} \right) \left[d\theta - \cos(2\theta) \sin(d\theta) \right] \hat{j} \\ &+ \frac{1}{2} d\phi \sin(2\theta) \sin(d\theta) \hat{k} \end{aligned}$$

In equation (18), \hat{i}, \hat{j} and \hat{k} are the unit basis vectors of the Cartesian coordinate system.

Equation (14) involves cell centre and faces values of intensity. A linear upwind scheme is used to interpolate the intensity at the face from the cell centre value (Coelho, 2014), then equation (14) is reduced to the standard algebraic form which can be solved by an iterative technique. To obtain the intensities, GAMG solver with symmetric Gauss-Seidel (symGaussSeidel) smoother is used (Parmananda et al., 2017).

The collimated feature has been developed in OpenFOAM framework and coupled with bBSF and named as buoyantBoussinesqCollimatedFoam (bBCF). The bBCF application has been used for numerical solutions and it requires extra information in the form of a boundary condition, which includes the irradiation value and beam direction, and the intensity on the boundary is computed using equation (9).

4 Non-dimensional parameters

The scales for length, velocity, temperature, conductive and radiative fluxes are $L, u_o, (T_{free} - T_c), \kappa(T_{free} - T_c)/L$

and σT_{free}^4 respectively, where $u_o = \sqrt{Lg\beta_T(T_{free} - T_c)}$ is convective velocity scale.

Thus, the non-dimensional quantities and parameters involved are as follows,

$$\begin{aligned} U_i &= \frac{u_i}{u_o}, \quad X_i = \frac{x_i}{L}, \quad \theta = \frac{T - T_c}{T_{free} - T_c}, \\ Ra &= \frac{g\beta_T(T_{free} - T_c)L^3}{\nu\alpha}, \quad Pr = \frac{\nu}{\alpha}, \\ N &= \frac{\kappa}{\sigma T_{free}^3 L}, \quad \tau = \kappa_a L, \quad Pl = N\tau. \end{aligned}$$

where Ra, Pr, N, Pl and τ are Rayleigh number, Prandtl number, conduction-radiation parameter, Planck number and optical thickness of the medium.

The non-dimensional irradiation is given as

$$\bar{G} = \frac{G}{\sigma T_{free}^4}, \quad (18)$$

The fluxes on the walls are presented into Nusselt number as

$$Nu_{cond} = \frac{q_{cond}L}{k(T_{free} - T_c)}, \quad Nu_{rad} = \frac{q_{rad}L}{k(T_{free} - T_c)}.$$

where, Nu_{cond} and Nu_{rad} , are conductive and radiative Nusselt numbers, respectively. q_{cond} and q_{rad} are conductive and radiative fluxes, respectively and L is the characteristic dimension of the present problem. Further, the total Nusselt number (Nu_t) is calculated as below

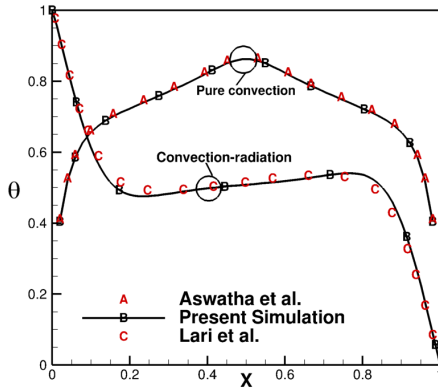
$$Nu_t = Nu_{cond} + Nu_{rad}.$$

5 Verification

5.1 Verification of pure convection

The bBSF without FVDM has been used to test the buoyancy flow for the symmetrical cooling case of natural convection. The pure convection graph in Figure 4 shows the temperature variation on the bottom wall of the cavity along with the result by Aswatha et al. (2013). The present result for pure convection agrees well with the published work.

Figure 4 The verification of results for pure convection in a square enclosure which is heated from the bottom (symbol A) and the combined diffuse radiation with natural convection in a square enclosure where differential temperature is applied on the two opposite vertical walls (symbol C) (see online version for colours)



5.2 Verification of diffuse and collimated beam radiation

The results by FVDOM are verified first for only radiation in a cavity having absorbing-emitting medium with $k_a = 0.1$ and 10 in a square enclosure as suggested by Raithby and Chui (1990). Figure 5 shows the variation of non-dimensional heat flux $q_r / \sigma T_h^4$ on the bottom wall and it matches well with the results of published work. Further, the collimated irradiation feature (Garg et al., 2019) has been tested in a square cavity as shown in Figure 6(a). The left side of the wall has a small window of non-dimensional size 0.05 at a non-dimensional height of 0.6. The walls of the square cavity are black and cold and also medium is non-participating. A collimated beam is irradiated on the window at an azimuthal 135° direction. It is expected that the beam would travel in an oblique direction of 135° angle without any attenuation and hit exactly a non-dimensional distance of 0.6 from the left wall. Figure 6(b) shows the contour of irradiation which clearly shows the travel of collimated without any attenuation.

Figure 5 The variation of non-dimensional heat flux on the bottom wall (see online version for colours)

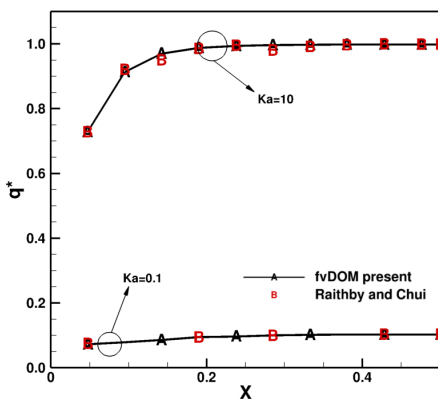
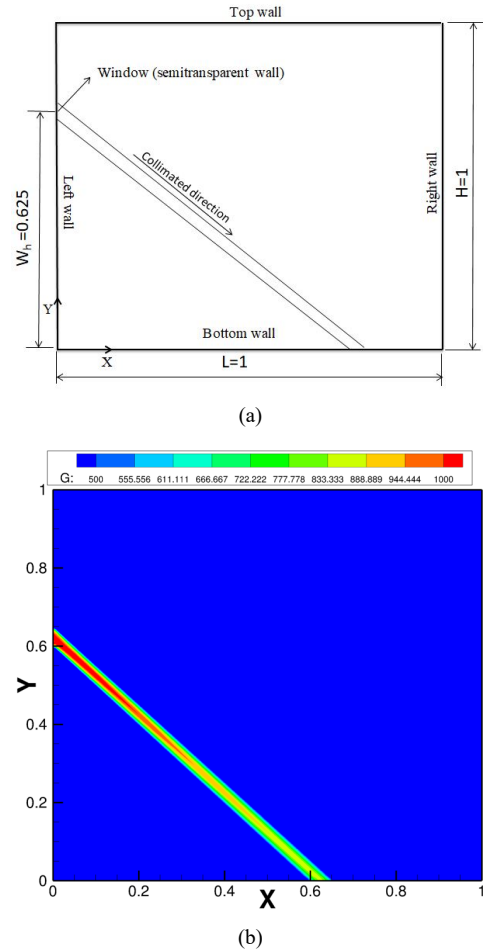


Figure 6 The verification of collimated beam feature, (a) test geometry (b) contour of irradiation showing the travel of the beam in transparent medium (see online version for colours)



5.3 Verification of combined natural convection and radiation

The bBSF is used to simulate diffuse radiation and natural convection in a square cavity whose top and bottom walls are adiabatic and vertical walls are isothermal at differential temperatures and radiatively opaque. The convective-radiative graph in Figure 4 shows the variation of temperature at mid height of the cavity for the present simulation in comparison with the results of Lari et al. (2011) and the accuracy of the present solver is in accordance with the published work.

6 Sensitivity tests of domain discretisation

The numerical solutions of Navier-Stokes, energy equations and radiation transfer equations are sensitive to spatial discretisation. Additionally, radiative transfer equation also requires angular space discretisation which provides directions along which radiation transfer equation is being solved. Thus, optimum number of grids and directions has been obtained through sensitivity test study in two steps:

Figure 7 The progression of collimated beam in (a) non-participating medium $Pl = 0$; participating medium for (b) $Pl = 1$ (c) $Pl = 10$ and (d) $Pl = 50$, for the irradiation value of $1,000 \text{ W/m}^2$ applied on the semitransparent wall for case A (see online version for colours)

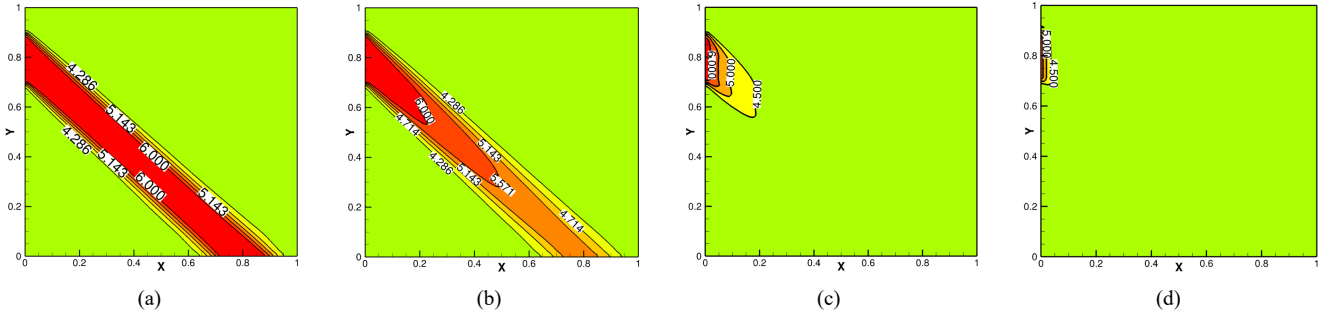


Figure 8 The contours of the non-dimensional stream function for (a) $Pl = 0$, (b) $Pl = 1$, (c) $Pl = 10$ and (d) $Pl = 50$ for case A (see online version for colours)

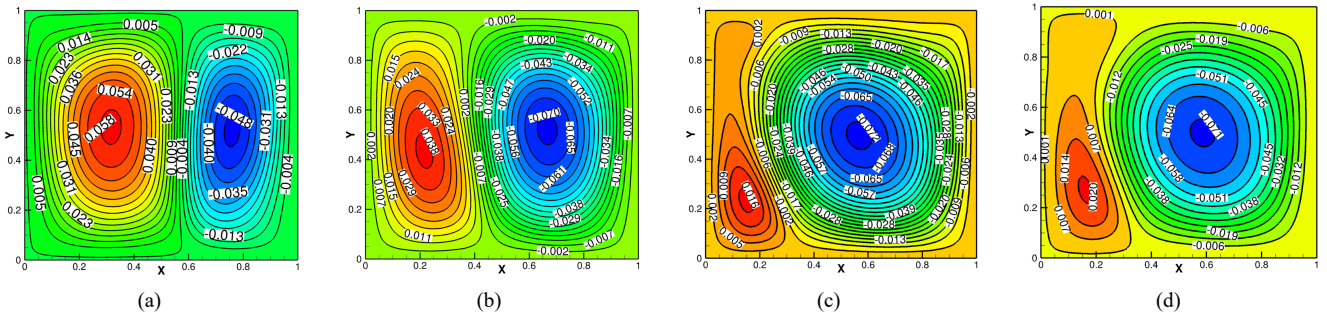
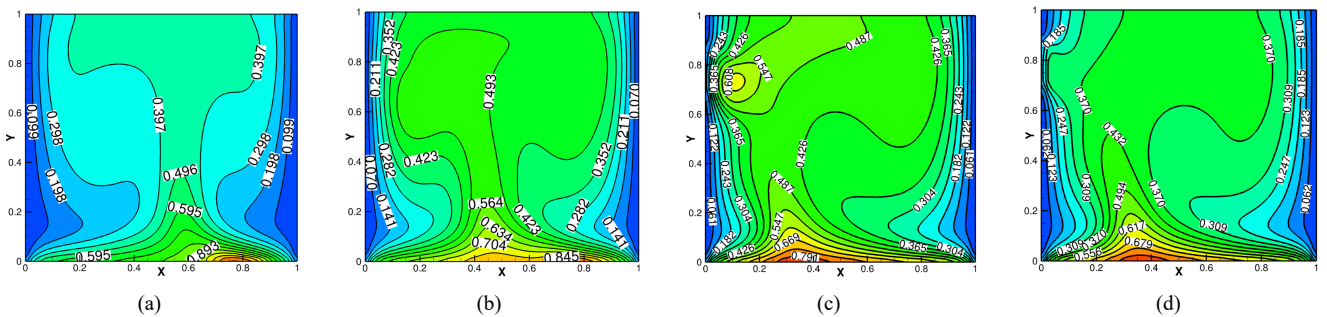


Figure 9 The non-dimensional temperature contours for (a) $Pl = 0$, (b) $Pl = 1$, (c) $Pl = 10$ and (d) $Pl = 50$ for case A (see online version for colours)



- 1 Spatial grids sensitivity test: three spatial grid sizes, i.e., 60×60 , 80×80 , and 100×100 are chosen to calculate the area average total Nusselt number on the bottom wall as shown in Table 1 for the present problem. The percentage error between the first and second grid sizes is 0.8%, whereas between second and third grid sizes is 0.15%. Thus, the spatial grid points, 80×80 is selected for the present study.
- 2 Angular direction sensitivity test: the polar (n_θ) discretisation does not have any effect in two-dimensional analysis, thus, it has been fixed to two for polar direction in OpenFOAM. The effect of angular discretisation on the area average total Nusselt number on the bottom wall is shown in Table 2. The percentage difference in area average Nusselt number

in the first and second angular discretisation is 0.09%, whereas in second and third angular discretisation is 0.22%. Thus, finally $n_\theta \times n_\phi = 2 \times 5$ in one quadrant angular space is selected for the study of the present problem.

Now, it is evident that the radiative transfer equation requires high computational resources. In order to quantify the time required to solve RTE in comparison to the solution of the convective transport equation the time stamping has been done for individual transport equations. It has been found that the solution of RTE takes around 91% time of the total simulation time.

7 Results and discussion

In the present numerical simulation, the parameters such as, Rayleigh number, Prandtl number, collimated irradiation and direction of collimated irradiation have been fixed to values 10^5 , 0.71, $G_{co} = 1,000 \text{ W/m}^2$, 135° , respectively. The simulations have been performed for the different aspect ratios of semitransparent window and Planck numbers and correspondingly, the fluid flow and the heat transfer characteristics are studied in the sections below.

Table 1 The area average total Nusselt number on the bottom wall

Nusselt number	60×60	80×80	100×100
Conduction	6.42	6.615	6.78
Radiation	-3.3	-3.47	-3.63
Total	3.12	3.145	3.15

Table 2 The area average total Nusselt number for angular discretisation on the bottom wall

Nusselt number	2×3	2×5	2×7
Conduction	6.617	6.513	6.687
Radiation	-3.47	-3.363	-3.53
Total	3.147	3.15	3.157

7.1 Case A: $h_r = 0.8$ and $w_r = 0.2$

A semitransparent window of width ratio of 0.2 is created at a height ratio of 0.8 on the left vertical wall. A collimated irradiation value of $1,000 \text{ W/m}^2$ is applied on this semitransparent window at an azimuthal angle of 135° . The dynamics of fluid flow and heat transfer for this case are described below.

The collimated beam progression into the cavity in azimuthal direction 135° from the semitransparent window can be best represented by irradiation contours. The irradiation contours inside the cavity for Planck numbers 0, 1, 10 and 50 are shown in Figures 7(a), 7(b), 7(c) and 7(d), respectively. The Planck number ($Pl = 0$) corresponds to a transparent medium, i.e., neither absorption nor emission happens by fluid therefore, the collimated irradiation value remains constant till it reaches the bottom wall. It spreads uniformly to the window width ratio of 0.2 and strikes the bottom wall at a non-dimensional distance of 0.7 from the left corner of the cavity. Whereas, the collimated irradiation reduces along the line of progression in a participating medium for non-zero Planck numbers of the medium. The collimated irradiation does not reach the bottom wall for $Pl = 10$ as can be seen from Figure 7(c). Moreover, the collimated beam energy gets absorbed near to the window for high optical thickness, i.e., $Pl = 50$ [see Figure 7(d)].

7.1.1 Characteristics of stream function and temperature fields

The effect of collimated beam irradiation on the stream function for Planck numbers 0, 1, 10 and 50 are shown in Figures 8(a)–8(d), respectively. Figure 8(a) depicts stream function contour for the transparent media, where two asymmetrical vortices can be observed. The left vortex is larger in size than the right vortex. As the medium behaves transparent for the radiation transfer, all collimated irradiation energy strikes on the bottom wall at a non-dimensional distance of 0.7 from the left corner with non-dimensional spread of 0.2. The 90% of the collimated energy is absorbed by ($\epsilon = 0.9$) the bottom wall, this causes the enhancement in the buoyancy force in the upward direction at this location (i.e., over the spread of collimated beam on the bottom wall), thus the resultant of momentum force and buoyancy vector is more in upward direction in the right vortex, thus making right vortex thinner and rest space is occupied by the left vortex. The reverse trend is observed for the participating media for Planck numbers $Pl = 1, 10$ and 50, where the left vortex is smaller in size than right vortex. This is due to the fact that collimated beam is travelling through the left vortex which absorbs the radiation energy and creates local heating in the fluid, this enhances local upward buoyancy force in the left vortex, whereas some energy is also being transferred to right vortex through absorption in the right vortex and also absorption by the bottom wall. The energy absorbed by the left vortex may be higher due to the large distance travelled by the collimated beam in the left vortex; this decreases the size of the left vortex and increases the size of the right vortex. The size of the left vortex keeps on decreasing till $Pl = 10$, afterwards its size increases. As the difference of two adjacent stream function values gives the mass flow rate (Darbandi and Abrar, 2014), the flow rate in the left vortex also keeps on decreasing till $Pl = 10$ and then increases. The reverse trend of this is found in the right vortex.

The effect of collimated beam radiation on the temperature field inside the cavity for the Planck number 0, 1, 10 and 50 are shown in Figures 9(a), 9(b), 9(c) and 9(d), respectively. The symmetrical isotherm lines about the mid vertical line of the cavity (Chanakya and Kumar, 2021a) becomes asymmetrical with inclusion of collimated beam and these lines tilt either right or left to the vertical line depending upon behaviour of the medium for the radiation. The isothermal lines are bent towards left for the participating medium as the left vortex is smaller in size (Figure 9). The clustering of isotherm lines appears at the strike zone at the bottom wall for non-participating medium, whereas almost uniform temperature is spread in the region near to the top adiabatic wall. Furthermore, density of the isotherm lines increases at the bottom and on left wall with the increase in Planck number of medium and also localised heating of the fluid is observed near to the semitransparent wall for the case $Pl = 10$ [see Figure 9(c)], this may be the fact that the most of collimated irradiation energy is getting absorbed within small distance

from the semitransparent wall [see Figure 7(c)], whereas the effect of localised heating is limited to semitransparent wall for the case of $Pl = 50$ [see Figure 9(d)], this is because of the fact that the almost all the collimated irradiation is absorbed near to semitransparent wall and the energy is transferred out from the cavity due to isothermal condition on the semitransparent wall. The maximum non-dimensional temperature inside the cavity is found on the bottom wall but at different locations for different Planck numbers; it is on the strike zone for Planck number 0 and 1, and at the junction point of two vortices for Planck number 10 and 50.

7.1.2 Velocity and temperature variations

The variations of non-dimensional vertical velocity in the horizontal direction at mid height of the cavity for the Planck numbers 0, 1, 10 and 50 are depicted in Figure 10. The vertical velocity is in the downward direction near to both the cold walls and reaches to maximum at same non-dimensional distance of 0.1 from the right vertical walls for all Planck numbers, however, this distance is 0.075 for Planck number 0 and 1, and 0.05 for Planck number 10 and 50 from the left wall. Furthermore, the vertical velocity in the downward directions keeps on decreasing away from the walls. The maximum non-dimensional temperature keeps on decreasing with increasing Planck number till $Pl = 10$ because heating near to top then little increase for $Pl = 50$ and reaches to zero at centre points of each vortex. The maximum non-dimensional vertical velocity in upward directions is achieved at the junction of two vortices.

The non-dimensional temperature on the bottom wall increases rapidly from the left end till the non-dimensional distance 0.1 afterwards its rate of increase is slow till the strike length of the collimated beam [Figure 11(a)]. Afterwards, there is a sudden rise in temperature at the strike zone and reaches a maximum value of non-dimensional temperature 1.4 then starts decreasing till the right wall for $Pl = 0$. For the case $Pl = 1$, two maximas in the temperature curve are observed that correspond to the strike length of the collimated beam and stagnation point developed at the junction of two vortices. Nevertheless, the location of the global maxima corresponding to the strike zone of the collimated beam remains fixed. It is the highest for the radiatively transparent fluid and keeps on decreasing with increasing Planck number of the medium. The high temperature zone due to collimated beam strike cannot be seen for Planck numbers 10 and 50, due to absorption of radiative energy within the fluid before it reaches to the bottom wall. The maximum non-dimensional temperature is found at the junction of two vortices (i.e., the stagnation point) for $Pl = 10$ and 50. The non-dimensional temperature on the top wall [Figure 11(b)] increases from both the ends of the wall upto distance of 0.2 and remains almost constant at the middle portion of the curve for $Pl = 1, 10$ and 50. However, a little decrease in temperature is seen at the

middle for $Pl = 0$. There is no major difference in the temperature profile observed for $Pl = 1$ and 10.

Figure 10 The variation of the non-dimensional vertical velocity along the horizontal line at the mid height of the cavity for various Planck numbers for case A (see online version for colours)

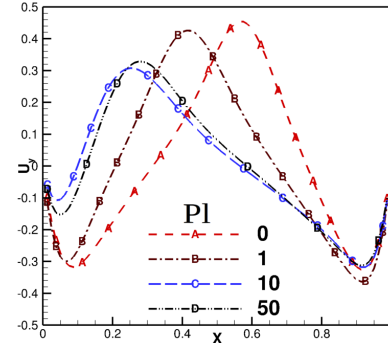
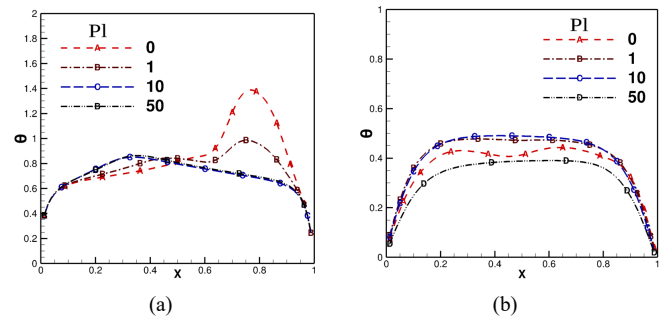


Figure 11 The variation of the non-dimensional temperature on, (a) bottom wall (b) top wall for various Planck numbers for case A (see online version for colours)



7.1.3 Variation of Nusselt number

The conduction (Nu_{cond}), radiation (Nu_{rad}) and total (Nu_{tot}) Nusselt numbers variation on the bottom wall are presented in Figure 12 for various values of Planck numbers. The variation of conduction Nusselt number on both ends of bottom wall are similar for all the Planck numbers, and its behaviour remains same till non-dimensional distance of 0.15 from the left corner and then slowly decreases to a minimum value of almost zero at a non-dimensional distance of 0.61 from left corner $Pl = 0$. All of a sudden, it increases to 16 at the strike length of the collimated beam, it further decreases to 9 then starts increasing and reaches to a maximum value of 17 on the right side of the isothermal wall for the case of the transparent medium. The lowest conduction Nusselt is obtained at distance of 0.4 and remains constant till the strike point of the collimated beam, then increases to a value of 8 for the case of $Pl = 1$. Further its behaviour is similar to the transparent medium case. Whereas, the conduction Nusselt number behaviour remains unaffected by the collimated beam for Planck numbers 10 and 50. However, Nu_{rad} remains constant for the values of $Pl = 0$ and 1 till a distance of 0.6 on the bottom wall, and an

inverted cone profile having a peak value of 22 and 7, are observed for the $Pl = 0$ and 1 respectively, whereas, the radiation Nusselt number remains constant over the entire length and its value is almost zero over the entire length of the bottom wall for the $Pl = 10$ and 50.

The total Nusselt number which is a linear combination of conduction and radiation Nusselt numbers is dominated by conduction Nusselt number over the most part of the bottom wall except the length over which collimated beam strikes [Figure 12(c)]. The total Nusselt number at the beam strike zone is dominated by the radiation Nusselt number. Whereas, no peak appears in the total Nusselt number for the Planck number 10 and 50 which further confirms that the collimated beam energy gets absorbed within the fluid before reaching to the bottom wall.

The variation of conduction, radiation and total Nusselt numbers on the left isothermal wall which also includes the semitransparent window for $Pl = 0, 1, 10$ and 50 are depicted in Figures 13(a), 13(b) and 13(c), respectively. There is sudden decrease in conduction Nusselt number over small height from the bottom and reaches to a minimum value of 1 and it almost remains constant over the rest height of the left wall for transparent medium cases. Nevertheless, small increment happens on the semitransparent wall for $Pl = 1$. However, there is a sudden increment in the conduction Nusselt number on the semitransparent window for $Pl = 10$ and 50. This is mostly in the negative direction which reveals that the energy leaves from this wall by the conduction mode of the heat transfer. The radiation Nusselt number is found to be almost zero over the height of the left wall except at the semitransparent wall. A sudden increase of radiation Nusselt number happens ($G = 1,000 \text{ W/m}^2$) at the semitransparent wall [Figure 13(b)] and remains the same for all Planck numbers. It is noticed that the radiative Nusselt number is positive; this reveals that the radiative heat flux is coming inside the cavity through radiation mode of heat transfer. The total Nusselt number on the left wall is negative over most part of the height indicates that energy is leaving from the domain except length of the semitransparent window, where the total Nusselt number is positive which indicates that the net energy is entering into the domain from this portion of the left wall.

The variation of conduction Nusselt number on the right wall [Figure 14(a)] is similar to the left wall except the phenomenon on the semitransparent window. There is no major change in the conduction Nusselt number on this wall with the Planck numbers of the medium. Nevertheless, the conduction Nusselt number increases little for $Pl = 1$ compared to $Pl = 0$, then decreases for $Pl = 10$ and $Pl = 50$. The radiation Nusselt number is almost constant over the whole height of the right wall and decreases with increase in Planck number. The radiation Nusselt number is almost zero for $Pl = 50$ on the right wall. The total Nusselt number is similar to the conduction Nusselt number curve, but the difference increases from $Pl = 1$ to $Pl = 50$.

7.2 Progression of collimated beam in other cases

The collimated irradiation contours for the aspect ratio of cases B, C, and D and for $Pl = 0$ are depicted in Figures 15(a), 15(b) and 15(c), respectively. The purpose of the present graph is to show the position of the semitransparent window and its width for different cases. The transparent medium has been selected to present the collimated beam contours, so that collimated irradiation contours remain the same throughout the progression of the beam. However, collimated beam contours will be different for different Planck numbers of the medium inside the cavity as shown Figure 7 nevertheless, they are not presented here for the brevity. The effects of these aspect ratios and Planck numbers of the medium on the fluid flow and the heat transfer will be presented in the subsequent sections.

7.3 Characteristics of the stream function and the temperature field in other cases

7.3.1 Case B: $h_r = 0.8$ $w_r = 0.4$

The effect of the collimated beam irradiation for the semitransparent window with aspect ratio $h_r = 0.8$ and $w_r = 0.4$ on the stream function for the range of Planck numbers 0–50 are depicted in Figure 16. The dynamics of two vortices are almost similar to case A (Figure 8), except little increase in the value of stream function, i.e., increase in the flow rate in respective vortices for Planck numbers 0 and 1, however, on further increase of the Planck number ($Pl = 10$) of the medium, the left vortex breaks into two parts upper left vortex and lower left vortex. The flow rate in the lower left vortex is higher than the upper left vortex. An interesting fact to notice that the flow rate in the right vortex also decreases. This upper left vortex disappears for Planck number $Pl = 50$ and flow rate in the lower left vortex also decreases. Nevertheless, the flow rate in the right vortex has now increased.

Figure 17 depicts the non-dimensional temperature contours for the range of Planck number $Pl = 0 - 50$. The qualitative behaviour for the case $Pl = 0$ [Figure 17(a)], is same as explained for Figure 9(a). Moreover, the local heating of the fluid happens near to the semitransparent wall for $Pl = 1$ [Figure 17(b)], this local heating further shifts near to the semitransparent wall for $Pl = 10$ and the density of the isothermal lines has also increased. Further, more temperature variations are seen in the upper region of the cavity. The local heating of the fluid does not happen for $Pl = 50$ as the maximum energy of the collimated beam gets absorbed near to the semitransparent wall and transferred out of the cavity as semitransparent wall is being isothermal. The clustering of isotherm lines near to the semitransparent window has also decreased. The location of the maximum temperature is at the beam strike zone at the bottom of the cavity for $Pl = 0$ and 1, however it is at the bottom wall at the junction of two vortices for $Pl = 10$ and 50.

Figure 12 The variation of, (a) conduction (b) radiation (c) total Nusselt numbers for different Planck numbers on the bottom wall for case A (see online version for colours)

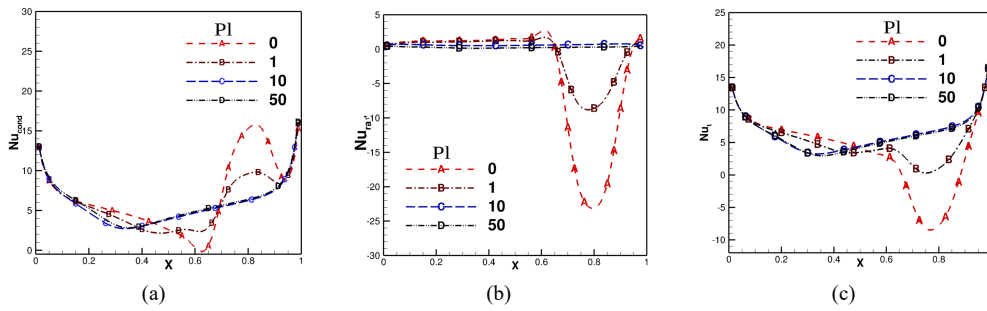


Figure 13 The variation of, (a) conduction (b) radiation (c) total Nusselt numbers for different Planck numbers on the left wall for case A (see online version for colours)

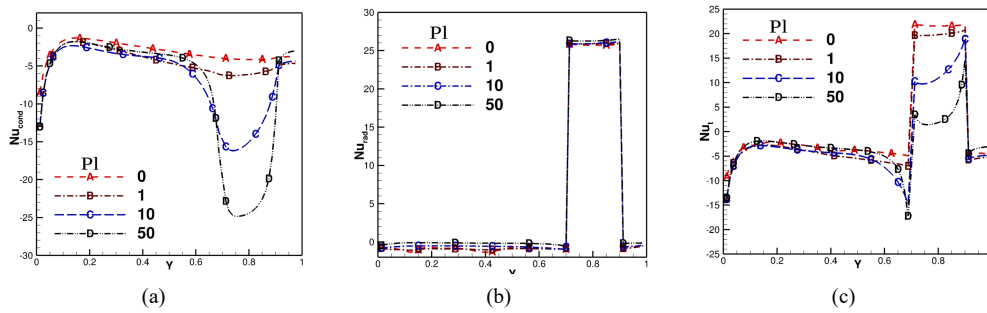


Figure 14 The variation of, (a) conduction (b) radiation (c) total Nusselt numbers for different Planck numbers on the right wall for case A (see online version for colours)

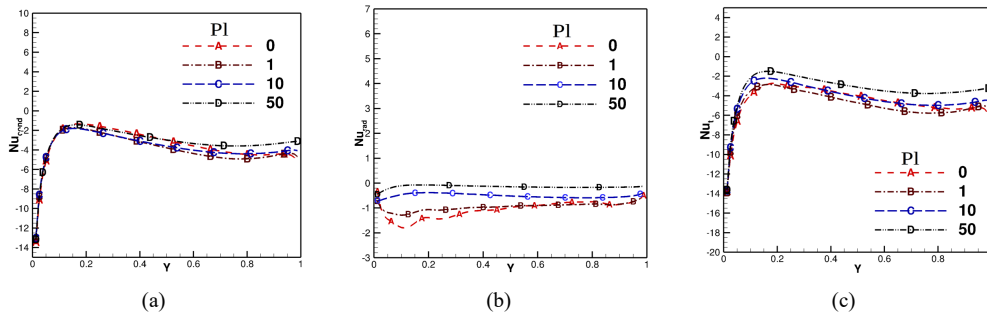


Figure 15 The progression of a collimated beam in a non-participating medium for, (a) case B: ($h_r = 0.8$ and $w_r = 0.4$) (b) case C: ($h_r = 0.4$ and $w_r = 0.2$) (c) case D: ($h_r = 0.4$ and $w_r = 0.4$) for the collimated irradiation value of $1,000 \text{ W/m}^2$ applied on the semitransparent wall at an azimuthal angle of 135° (see online version for colours)

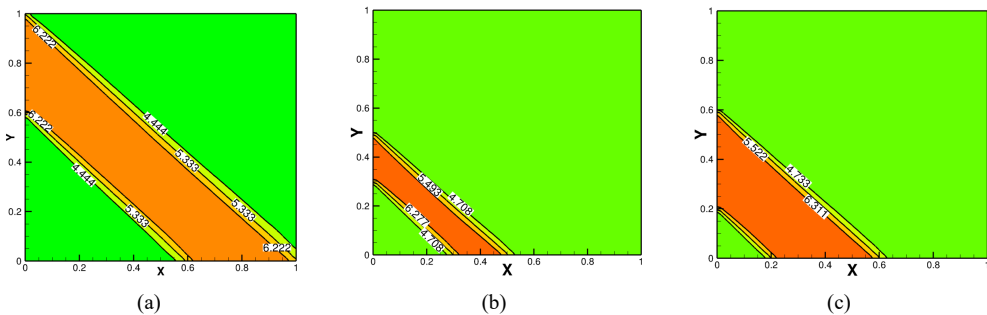


Figure 16 The contours of the non-dimensional stream function for, (a) $Pl = 0$ (b) $Pl = 1$ (c) $Pl = 10$ (d) $Pl = 50$ for case B (see online version for colours)

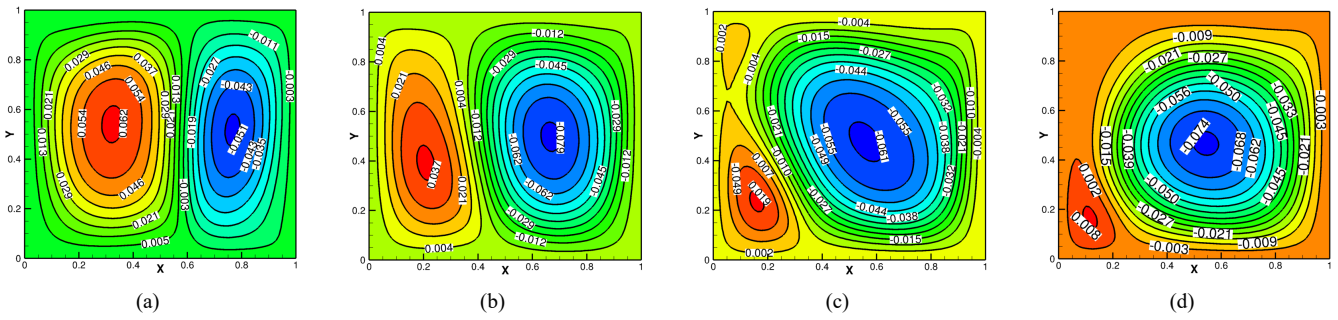


Figure 17 The contours of the non-dimensional temperature for, (a) $Pl = 0$ (b) $Pl = 1$ (c) $Pl = 10$ (d) $Pl = 50$ for case B (see online version for colours)

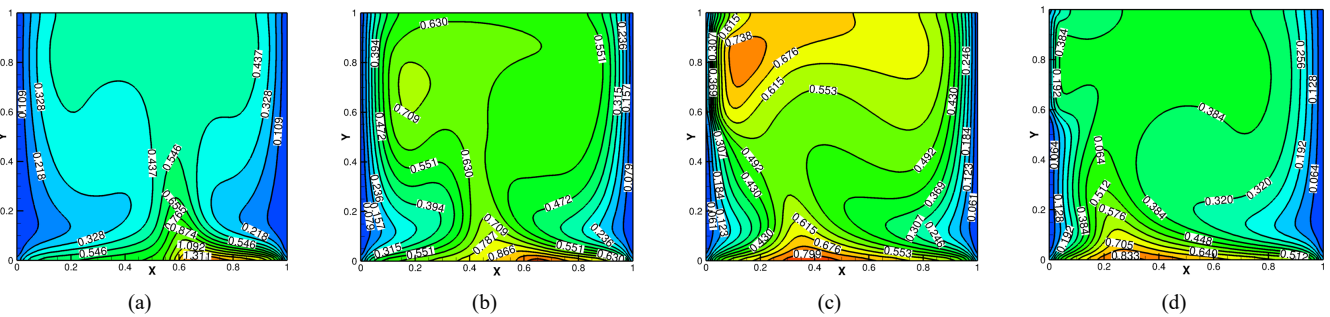


Figure 18 The contours of the non-dimensional stream function for, (a) $Pl = 0$ (b) $Pl = 1$ (c) $Pl = 10$ (d) $Pl = 50$ for case C (see online version for colours)

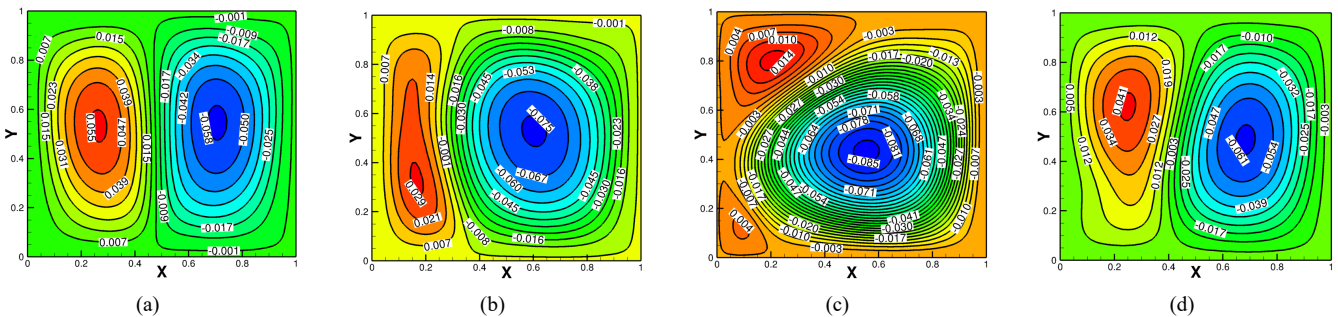


Figure 19 The contours of the non-dimensional temperature for, (a) $Pl = 0$ (b) $Pl = 1$ (c) $Pl = 10$ (d) $Pl = 50$ for case C (see online version for colours)

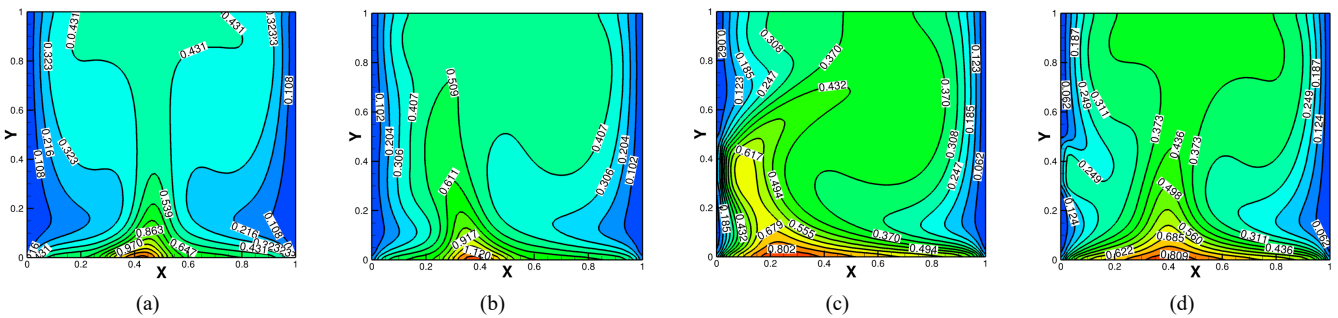


Figure 20 The contours of the non-dimensional stream function for, (a) $Pl = 0$ (b) $Pl = 1$ (c) $Pl = 10$ (d) $Pl = 50$ for case D (see online version for colours)

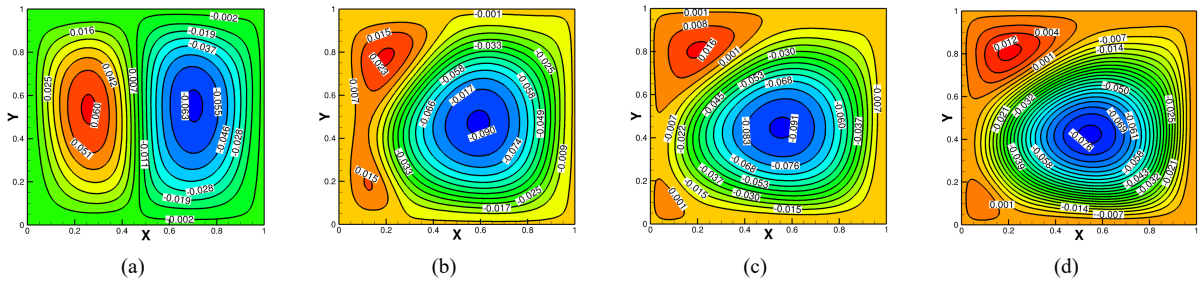


Figure 21 The contours of the non-dimensional temperature for, (a) $Pl = 0$ (b) $Pl = 1$ (c) $Pl = 10$ (d) $Pl = 50$ for case D (see online version for colours)

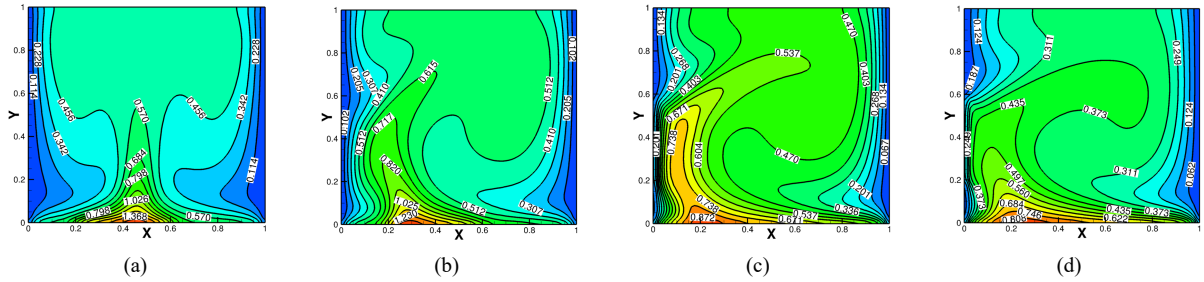


Figure 22 The variations of the non-dimensional temperature on the bottom wall for, (a) $Pl = 0$ (b) $Pl = 1$ (c) $Pl = 10$ (d) $Pl = 50$ (see online version for colours)

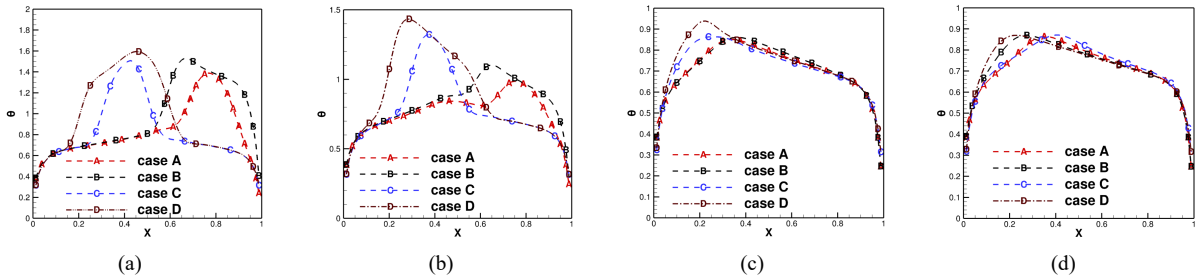


Figure 23 The variation of the conduction Nusselt number on the bottom wall for the different cases for (a) $Pl = 0$ (b) $Pl = 1$ (c) $Pl = 10$ (d) $Pl = 50$ (see online version for colours)

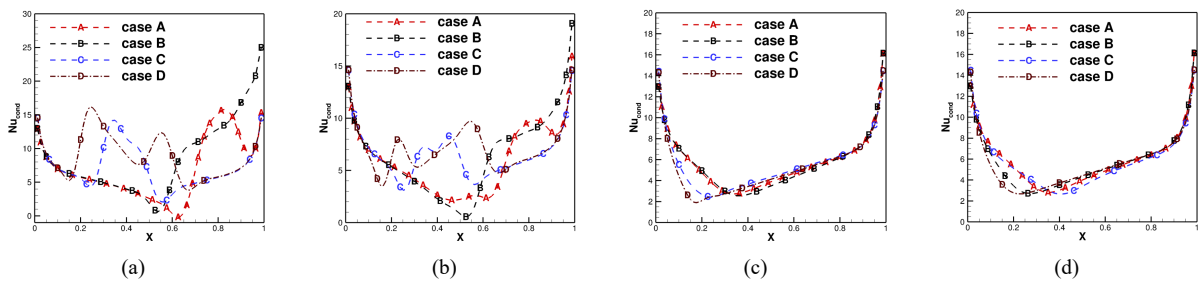
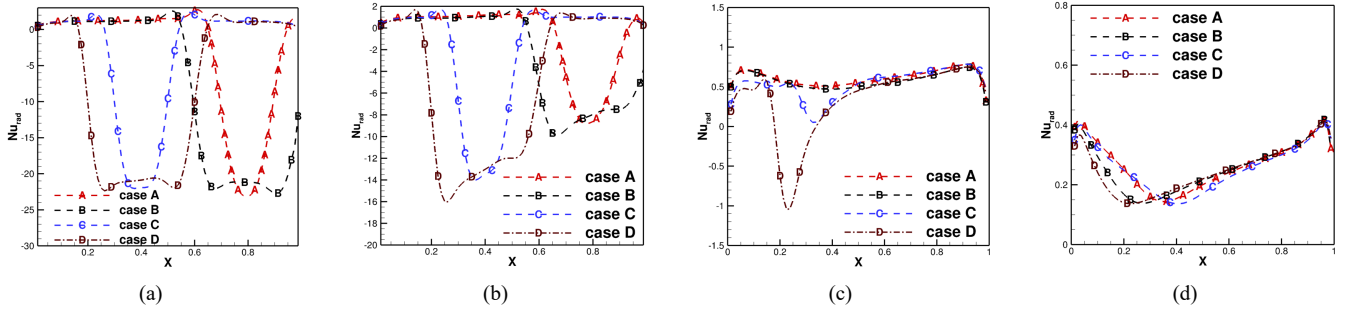


Table 3 The non-dimensional maximum stream function values for various cases over the range of Planck numbers

Pl	Case A		Case B		Case C		Case D				
	Left	Right	Left	Right	Left	Right	Left	Right			
0	0.052	-0.043	0.062	-0.051	0.055	-0.058	0.060	-0.063			
1	0.032	-0.064	0.037	-0.079	0.029	-0.075	0.015(b)	0.023(t)	-0.090		
10	0.013	-0.068	0.019(b)	0.002(t)	-0.061	0.004(b)	0.014(t)	-0.085	0.001(b)	0.016(t)	-0.091
50	0.020	-0.071	0.008	-0.071	0.041	-0.061	0.001(b)	0.012(t)	-0.076		

Figure 24 The variation of the radiation Nusselt number on the bottom wall for the different cases for, (a) $Pl = 0$ (b) $Pl = 1$ (c) $Pl = 10$ (d) $Pl = 50$ (see online version for colours)



7.3.2 Case C: $h_r = 0.4$ $w_r = 0.2$

Unlike to cases A and B for the transparent medium ($Pl = 0$) the left vortex is little smaller in size to the right side vortex for this case [compares Figures 8(a), 16(a) to 18(a)]. This is mainly due to the fact that the collimated beam incidence takes place between the non-dimensional length 0.3 to 0.5 on the bottom wall. This incidence length is below to the left vortex, thus higher buoyancy causes the resultant force (momentum and buoyancy) vector more in vertical direction, thus, reduction of size of the left vortex. One interesting fact to notice is that fluid velocity has almost 90° turn in the right vortex at the end point of collimated strike. Also, the flow rate (difference of two stream function values) in the right vortex is higher than the left vortex unlike cases A and B for transparent medium. The flow rate in the right vortex keeps on increasing with increase of Planck number of the medium till $Pl = 10$. The size of the left vortex also keeps on decreasing with the Planck number of the medium and the left vortex breaks into two parts for $Pl = 10$. However, a totally different situation appears for these two vortices for $Pl = 50$. The left vortex has grown and the right vortex has reduced in the size. The flow rate in the left vortex has also increased whereas, it is reduced in the right vortex.

The plume is rising from the collimated incidence length and it is almost vertical for the transparent medium ($Pl = 0$) [Figure 19(a)], this plume is bent towards the left for Planck number ($Pl = 1$) [see Figure 19(b)] case. Further, it gets more bent and nearly touches the left isothermal wall for Planck number $Pl = 10$ [see Figure 19(c)]. On contrary to this, the plume is bent toward the right for $Pl = 50$ [see Figure 19(d)]. The isotherm lines are also clustered and parallel to the semitransparent window for Planck number $Pl = 50$. In this case also, the maximum temperature exists on the bottom wall like cases A and B and is at the point of incident of the collimated beam for Planck number 0 and 1 and at the junction point two vortices on the bottom wall for $Pl = 10$ and 50.

7.4 Case D: $h_r = 0.4$ $w_r = 0.4$

There is no major change seen in the fluid flow behaviour with the increase of window width ratio for the transparent

medium case compared to case C (Figure 20). Nevertheless, the flow rate in both the vortices increases [compare Figures 18(a) and 20(a)]. However, the size of the left vortex reduces drastically for $Pl = 1$ and breaks into two parts-upper left vortex and lower left vortex but both remain connected. Furthermore, they are disconnected for $Pl = 10$. The lower left vortex has lower flow rate compared to the upper left vortex, also the flow rate in the right vortex increases. On further increase of the optical thickness of the medium ($Pl = 50$), the flow rates in the right vortex and upper left vortex decrease and there is no change in lower left vortex.

Similarly, no major change in the temperature contours (Figure 21) appear for the transparent and the participating medium cases compared to case C except the plume is bent towards the left wall for $Pl = 50$ case [compare Figures 18(d) and 20(d)]. The isotherm lines are parallel and closely packed near to the semitransparent window.

7.5 Variation of non-dimensional temperature profile in other cases

Figure 22 depicts the non-dimensional temperature variation on the bottom wall for the different cases, also for the range of Planck numbers of the medium. The peak of the temperature profile shifts to the left from case A to C and for Planck numbers 0 and 1, whereas the temperature profile almost remains same for case A and B for Planck number 10. Furthermore, no ordered way of shifting of temperature peak appears for the different cases for Planck number 50.

The maximum non-dimensional stream function value in a vortex for $Pl = 0$ to 50 and all cases have been presented in Table 3. As the left vortex breaks into two parts in some cases, therefore, the stream function value of these two vortices have been shown in table by bifurcating the cell into two parts. The first bifurcated part shows the stream function value of the upper left vortex and second bifurcated part shows the stream function value of the lower left vortex. There is no monotonic order for increasing or decreasing of these stream function values. The maximum and minimum values of the stream function are found right vortex for Planck number 10 for case D, and left vortex for Planck number 0 and case B.

Similarly, the maximum non-dimensional temperature inside the cavity is shown in Table 4. In a few scenarios, the maximum non-dimensional temperature has increased beyond one. The maximum non-dimensional temperature is found for case D and $Pl = 0$, and the minimum non-dimensional temperature is found for case A and $Pl = 10$.

Table 4 The maximum non-dimensional temperature inside the cavity for different cases over a range of Planck numbers

Pl	Case A	Case B	Case C	Case D
0	1.388	1.529	1.509	1.596
1	0.986	1.102	1.324	1.434
10	0.851	0.860	0.863	0.939
50	0.864	0.869	0.872	0.870

7.5.1 Variation of Nusselt number in other cases

Figure 23 shows the variation of conduction Nusselt number on the bottom wall for different cases and for a range of Planck numbers. The conduction Nusselt number goes to minimum (almost zero) before the strike length of collimated beam, rises to maximum ($Nu_{cond} = 16$) in the strike length, and decreases at the end of the strike length then goes up till end of the bottom wall for case A and for Planck number zero [see Figure 23(a)]. Similarly, the minimum conduction Nusselt number ($Nu_{cond} = 1$) is obtained just before strike point of the collimated beam for case B and for $Pl = 0$, afterwards, the sharp rise in the conduction Nusselt number curve appears at the start of the strike zone of the collimated beam for case B, and afterward low rate of increase in conduction Nusselt number happens and finally the highest Nusselt number is achieved at the end. Moreover, the minimum conduction Nusselt number ($Nu_{cond} = 3$) is obtained at the end of the strike point for case C for $Pl = 0$. The conduction Nusselt number curve has two peaks in the strike zone of the collimated beam for case D and $Pl = 0$. The characteristics of conduction Nusselt number graph for $Pl = 1$ and all the cases are similar to non-participating medium ($Pl = 0$) except peak and trough of the curve in the strike zone of the collimated beam have reduced. These peaks have disappeared for Planck number $Pl = 10$. The minimum point in the conduction Nusselt number curve is same for case A and B, however, it shifts to the left for case C and further shifting to left happens for case D. Other than the inflection point, the conduction Nusselt number curve remains same for all cases. The similar behaviour is observed for $Pl = 50$. One interesting fact to notice is that conduction Nusselt number behaviour for cases A and C is similar and for cases B and D. The minimum Nusselt number obtained is 2 for $Pl = 10$ and 50, and maximum is 16 which is obtained at the right end of the bottom wall.

The radiative Nusselt number distribution on the bottom wall for different cases and range of $Pl = 0 - 50$ is presented in Figure 24. The radiative Nusselt number is almost zero over the length of the bottom wall except

the length over which the collimated beam strikes. The Gaussian profile of radiative Nusselt number in the collimated beam strike zone appears for cases A and C, where it is almost square profile for cases B and D. The front of the square shape of radiative Nusselt number is not flat but wavy which has peak at the corner and trough at the middle. Moreover, the maximum value of radiative Nusselt number is almost same for all cases for Planck number zero [Figure 24(a)]. The profile of the radiative Nusselt number curve for different cases are retained for $Pl = 1$ [Figure 24(b)], however, maximum value of radiative Nusselt number is monotonically increasing from case A to case D. One interesting fact to notice that front of these profile are also tilted which has higher value at the start of the strike zone of the collimated beam and lower value at end of the beam. The peaks in the radiative Nusselt number curve disappear for cases A and B [Figure 24(c)] for $Pl = 10$, however, the profile for case C and D become Gaussian where case D has higher value of radiation Nusselt number than the case C. Furthermore, these peaks disappear in cases C and D [see Figure 24(d)].

Table 5 shows the area average conduction, radiation and total Nusselt numbers on the bottom wall of the cavity. The average conduction Nusselt number decreases upto $Pl = 10$ then there is slight increase in the average total Nusselt number whereas average radiative Nusselt number first being negative for ($Pl = 0$ and 1) then becomes positive for ($Pl = 10$ and 50) for all cases. Furthermore, average Nusselt number increases upto $Pl = 10$ and then there is minimal decrease in the average Nusselt number for all cases. The minimum value of average total Nusselt number is found for $Pl = 0$ and for case B and the maximum for $Pl = 10$ for case A.

The area average conduction, radiation and total Nusselt numbers on the right and the left walls excluding the semitransparent window are presented in Table 6 and 7, respectively. Both the conduction and the radiative Nusselt numbers are negative on both the walls for all cases and all Planck numbers. The average conduction Nusselt number increases upto Planck number $Pl = 1$ on the right wall and $Pl = 10$ on the left wall for all cases. However, average radiation Nusselt number monotonically decreases with Planck number for all the cases.

The area average conduction, radiation and total Nusselt number on the semitransparent wall for all the cases and range of Planck numbers are depicted in Table 8. The conduction Nusselt number is always negative and increases with increase of the Planck number of the medium for all cases. While the radiative Nusselt number is positive and almost constant for all Planck numbers in each case. One thing to notice is that radiative Nusselt number is same for case A and C and similarly it is same for cases B and D. The maximum conduction Nusselt number is found for case D for Planck number $Pl = 50$. The maximum and minimum total Nusselt number on the semitransparent wall are found for case D for $Pl = 0$ and $Pl = 50$, respectively.

Table 5 The area average Nusselt numbers on the bottom wall for different cases and the range of Planck numbers

Pl	Case A			Case B			Case C			Case D		
	Cond	Rad	Tot									
0	6.513	-3.363	3.033	8.13	-7.709	0.421	7.126	-3.296	3.83	8.718	-7.97	0.748
1	5.712	-0.712	5	6.332	-2.835	3.497	6.422	-1.867	4.555	7.021	-4.882	2.139
10	5.643	0.610	6.254	5.546	0.574	6.12	5.632	0.118	5.75	5.154	0.338	5.492
50	5.845	0.264	6.109	5.653	0.254	5.907	5.663	0.066	5.699	5.513	0.248	5.761

Table 6 The area average Nusselt numbers for on the right wall for different cases and range of Planck numbers

Pl	Case A			Case B			Case C			Case D		
	Cond	Rad	Tot									
0	-3.380	-1.045	-4.425	-4.385	-1.569	-5.954	-3.641	-0.939	-4.58	-4.354	-1.267	-5.621
1	-3.831	-0.940	-4.771	-5.265	-1.287	-6.552	-3.899	-0.892	-4.791	-4.863	-1.097	-5.96
10	-3.619	-0.499	-4.118	-4.924	-0.641	-5.565	-3.298	-0.44	-3.738	-4.397	-0.59	-4.987
50	-3.046	-0.142	-3.188	-3.033	-0.141	-3.174	-3.18	-0.144	-3.324	-2.956	-0.135	-3.091

Table 7 The area average Nusselt numbers on the left wall for different cases and range of Planck numbers

Pl	Case A			Case B			Case C			Case D		
	Cond	Rad	Tot									
0	-2.258	-0.688	-2.946	-1.875	-0.669	-2.544	-3.046	-0.764	-3.81	-3.136	-0.694	-3.83
1	-3.424	-0.814	-4.238	-2.984	-0.666	-3.65	-3.251	-0.767	-4.018	-3.05	-0.691	-3.74
10	-3.92	-0.574	-4.494	-3.313	-0.407	-3.72	-3.621	-0.443	-4.055	-3.433	-0.429	-3.862
50	-3.188	-3.361	-0.138	-2.831	-0.126	-2.957	-3.272	-0.162	-3.439	-2.586	-0.141	-2.727

Table 8 The area average Nusselt numbers on the semitransparent window for different cases and range of Planck numbers

Pl	Case A			Case B			Case C			Case D		
	Cond	Rad	Tot	Cond	Rad	Tot	Cond	Rad	Tot	Cond	Rad	Tot
0	-0.816	5.152	4.336	-1.848	9.94	8.092	-0.537	5.102	4.565	-1.351	10.055	8.704
1	-1.194	5.182	3.988	-3.2	9.953	6.723	-0.862	5.12	4.258	-2.558	10.123	7.564
10	-2.738	5.195	2.457	-6.757	9.943	3.186	-3.01	5.166	2.036	-6.87	10.23	3.36
50	-4.489	5.166	0.677	-9.858	10.169	0.311	-4.197	5.265	1.068	-10.375	10.435	0.062

8 Conclusions

The effects of the aspect ratio of the semitransparent window on the interaction of collimated beam with natural convection have been studied for $Ra = 10^5$, $Pr = 0.71$, $N = 1.5$ and $G = 1,000 \text{ W/m}^2$ numerically in a square cavity which is heated from the bottom. The four combinations of height ratio (h_r) and window width ratio (w_r) and range of Planck numbers have been considered. A collimated beam is irradiated on this semitransparent window at an azimuthal angle 135° and the interaction of this collimated beam irradiation with natural convection is considered through one way coupling. The following conclusions are drawn:

- 1 The left vortex is bigger in size than the right vortex for cases A and B for transparent medium $Pl = 0$. Furthermore, the fluid flow turns to almost right

angle for right vortex at the junction of two vortices for cases C and D.

- 2 The left vortex changes its dynamics with Planck number of the participating medium. It breaks into two parts for cases B, C and D for Planck number $Pl = 10$. Moreover, the left vortex remains confined into lower left corner for case B and breaks into two part for case D for $Pl = 50$.
- 3 The thermal plume flickers right to left as medium changes from non-participating to participating medium for all cases except Planck number $Pl = 50$ and case C where thermal plume is bent to the right.
- 4 The local heating of the fluid occurs by collimated beam for $Pl = 10$ for case A and $Pl = 1$ and 10 for case B.

- 5 The temperature rise on the bottom wall happens in increasing order from case A to case D at the location of collimated incidence for transparent medium case and this rise diminishes in the same order for $Pl = 1$, and finally no major rise in the temperature at the bottom wall appear for $Pl = 50$.
- 6 The maximum non-dimensional temperature inside the cavity increases beyond one, and maximum non-dimensional temperature is found for $Pl = 0$ of case D, and minimum for $Pl = 10$ of case A.
- 7 The conduction Nusselt number profile is Gaussian for case A at the collimated incidence location on the bottom wall and square for case D for transparent medium. The peak in the curve of conduction Nusselt number is at the incidence location and diminishes fast and no such peak is seen for all cases for $Pl = 50$.
- 8 The radiative Nusselt number rises all of sudden at the collimated beam incidence on the bottom wall and is almost same for all cases for transparent medium case. However, nature of this curve is Gaussian for case A and C and square for B and D, nevertheless, the front of the square curve is wavy with peak at the ends and trough at the middle.
- 9 The sudden rise in the radiation Nusselt number diminishes fast from case D to case A for $Pl = 1$ and no such rise appears for $Pl = 50$.
- 10 The maximum Nusselt number 5.76 is found for $Pl = 50$ and case D, and minimum total Nusselt number 0.42 is for $Pl = 0$ and case B on the bottom wall.

Acknowledgements

The authors greatly acknowledge the financial support provided by the Science and Engineering Research Board (SERB) (Statutory Body of the Government of India) via Grant No.: ECR/2015/000327 to carry out the present work.

References

- Abdallah, P.B. and Le Dez, V. (2000) 'Radiative flux field inside an absorbing-emitting semi-transparent slab with variable spatial refractive index at radiative conductive coupling', *Journal of Quantitative Spectroscopy and Radiative Transfer*, Vol. 67, No. 2, pp.125–137.
- Aswatha, M., Gangadhara Gowda, C.J., Sridhara, S.N. and Seetharamu, K.N. (2013) 'Effect of convective boundary conditions at bottom wall on natural convection in a square cavity', *Journal of Engineering Science and Technology*, Vol. 8, No. 2, pp.141–164.
- Aydin, O. and Yang, W.-J. (2000) 'Natural convection in enclosures with localized heating from below and symmetrical cooling from sides', *International Journal of Numerical Methods for Heat & Fluid Flow*, Vol. 10, No. 5, pp.518–529.
- Bees, M.A. (2020) 'Advances in bioconvection', *Annual Review of Fluid Mechanics*, Vol. 52, pp.449–476.
- Calcagni, B., Marsili, F. and Paroncini, M. (2005) 'Natural convective heat transfer in square enclosures heated from below', *Applied Thermal Engineering*, Vol. 25, No. 16, pp.2522–2531.
- Chai, J.C., Lee, H.S. and Patankar, S.V. (1993) 'Ray effect and false scattering in the discrete ordinates method', *Numerical Heat Transfer, Part B Fundamentals*, Vol. 24, No. 4, pp.373–389.
- Chanakya, G. and Kumar, P. (2021a) 'Effects of diffuse and collimated beam radiation on a symmetrical cooling case of natural convection', *Thermal Science and Engineering Progress*, Vol. 25, p.101006.
- Chanakya, G. and Kumar, P. (2021b) 'Investigation of thermal adiabatic boundary condition on semitransparent wall in combined radiation and natural convection', *International Journal for Computational Methods in Engineering Science and Mechanics*, pp.1–18.
- Chui, E. and Raithby, G. (1993) 'Computation of radiant heat transfer on a nonorthogonal mesh using the finite-volume method', *Numerical Heat Transfer*, Vol. 23, No. 3, pp.269–288.
- Coelho, P.J. (2014) 'Advances in the discrete ordinates and finite volume methods for the solution of radiative heat transfer problems in participating media', *Journal of Quantitative Spectroscopy and Radiative Transfer*, Vol. 145, pp.121–146.
- Darbandi, M. and Abrar, B. (2014) 'A compressible approach to solve combined natural convection-radiation heat transfer in participating media', *Numerical Heat Transfer, Part B: Fundamentals*, Vol. 66, No. 5, pp.446–469.
- Das, D., Roy, M. and Basak, T. (2017) 'Studies on natural convection within enclosures of various (non-square) shapes – a review', *International Journal of Heat and Mass Transfer*, Vol. 106, pp.356–406.
- Fu, L., Zhang, W., Ming, P., Zhang, M. and Ni, D. (2015) 'Natural convection coupled with radiation heat transfer in slanted square and shallow enclosures containing an isotropic scattering medium', *Numerical Heat Transfer, Part A: Applications*, Vol. 68, No. 12, pp.1369–1393.
- Ganzarolli, M.M. and Milanez, L.F. (1995) 'Natural convection in rectangular enclosures heated from below and symmetrically cooled from the sides', *International Journal of Heat and Mass Transfer*, Vol. 38, No. 6, pp.1063–1073.
- Garg, A., Chanakya, G. and Kumar, P. (2019) 'Numerical error estimation in finite volume method for radiative transfer equation for collimated irradiation', *Proceedings of the 9th International Symposium on Radiative Transfer, RAD-19*.
- Hasnaoui, M., Bilgen, E. and Vasseur, P. (1992) 'Natural convection heat transfer in rectangular cavities partially heated from below', *Journal of Thermophysics and Heat transfer*, Vol. 6, No. 2, pp.255–264.
- Karatas, H. and Derbentli, T. (2018) 'Natural convection and radiation in rectangular cavities with one active vertical wall', *International Journal of Thermal Sciences*, Vol. 123, pp.129–139.
- Kong, B. and Vigil, R.D. (2014) 'Simulation of photosynthetically active radiation distribution in algal photobioreactors using a multidimensional spectral radiation model', *Bioresource Technology*, Vol. 158, pp.141–148.
- Krishna, N.A. and Mishra, S.C. (2006) 'Discrete transfer method applied to radiative transfer in a variable refractive index semitransparent medium', *Journal of Quantitative Spectroscopy and Radiative Transfer*, Vol. 102, No. 3, pp.432–440.

- Kumar, P. and Eswaran, V. (2013) 'The effect of radiation on natural convection in slanted cavities of angle $\gamma = 45$ and 60° ', *International Journal of Thermal Sciences*, Vol. 67, pp.96–106.
- Lari, K., Baneshi, M., Nassab, S.G., Komiya, A. and Maruyama, S. (2011) 'Combined heat transfer of radiation and natural convection in a square cavity containing participating gases', *International Journal of Heat and Mass Transfer*, Vol. 54, Nos. 23–24, pp.5087–5099.
- Mezrhab, A., Bouali, H., Amaoui, H. and Bouzidi, M. (2006) 'Computation of combined natural-convection and radiation heat-transfer in a cavity having a square body at its center', *Applied Energy*, Vol. 83, No. 9, pp.1004–1023.
- Modest, M.F. (2013) *Radiative Heat Transfer*, Academic Press.
- Mondal, B. and Mishra, S.C. (2008) 'Simulation of natural convection in the presence of volumetric radiation using the lattice Boltzmann method', *Numerical Heat Transfer, Part A: Applications*, Vol. 55, No. 1, pp.18–41.
- Moukalled, F., Mangani, L. and Darwish, M. (2016) *The Finite Volume Method in Computational Fluid Dynamics*, Vol. 113, Springer.
- OpenFOAM (2017) *The Open Source CFD Toolbox: User Guide*, OpenFOAM v1706.
- Panda, M. (2020) 'Effects of anisotropic scattering on the onset of phototactic bioconvection with diffuse and collimated irradiation', *Physics of Fluids*, Vol. 32, No. 9, pp.091903.
- Panda, M., Singh, R., Mishra, A.C. and Mohanty, S.K. (2016) 'Effects of both diffuse and collimated incident radiation on phototactic bioconvection', *Physics of Fluids*, Vol. 28, No. 12, p.124104.
- Parmananda, M., Khan, S., Dalal, A. and Natarajan, G. (2017) 'Critical assessment of numerical algorithms for convective-radiative heat transfer in enclosures with different geometries', *International Journal of Heat and Mass Transfer*, Vol. 108, pp.627–644.
- Patankar, S.V. (2018) *Numerical Heat Transfer and Fluid Flow*, CRC Press.
- Rahimi, A., Saeed, A.D., Kasaeipoor, A. and Malekshah, E.H. (2019) 'A comprehensive review on natural convection flow and heat transfer: the most practical geometries for engineering applications', *International Journal of Numerical Methods for Heat & Fluid Flow*.
- Raithby, G. and Chui, E. (1990) 'A finite-volume method for predicting a radiant heat transfer in enclosures with participating media', *J. Heat Transfer*, Vol. 112, No. 2, pp.415–423.
- Sun, H., Chénier, E. and Lauriat, G. (2011) 'Effect of surface radiation on the breakdown of steady natural convection flows in a square, air-filled cavity containing a centered inner body', *Applied Thermal Engineering*, Vol. 31, Nos. 6–7, pp.1252–1262.
- Sun, Y., Zhang, X. and Howell, J.R. (2017) 'Assessment of different radiative transfer equation solvers for combined natural convection and radiation heat transfer problems', *Journal of Quantitative Spectroscopy and Radiative Transfer*, Vol. 194, pp.31–46.
- Verma, A.K., Rath, P. and Mahapatra, S. (2016) 'Interaction of short pulse collimated irradiation with inhomogeneity: an accurate model', *International Communications in Heat and Mass Transfer*, Vol. 72, pp.1–9.
- Vincent, R. and Hill, N. (1996) 'Bioconvection in a suspension of phototactic algae', *Journal of Fluid Mechanics*, Vol. 327, pp.343–371.
- Webb, B. and Viskanta, R. (1987) 'Radiation-induced buoyancy-driven flow in rectangular enclosures: experiment and analysis', *Journal of Heat Transfer*, Vol. 109, No. 2, pp.427–433.
- Yigit, S., Poole, R.J. and Chakraborty, N. (2015) 'Effects of aspect ratio on natural convection of bingham fluids in rectangular enclosures with differentially heated horizontal walls heated from below', *International Journal of Heat and Mass Transfer*, Vol. 80, pp.727–736.

Nomenclatures

Acronyms	
a	Coefficient
C_p	Specific heat capacity (J/kgK)
g	Acceleration due to gravity (m/s^2)
$bBSF$	buoyantBoussinesqSimpleFoam
$bBCF$	buoyantBoussinesqCollimatedFoam
RTE	Radiative transfer equation
$DILU$	Diagonal incomplete LU decomposition
$GAMG$	Geometric-algebraic multi-grid
DIC	Diagonal incomplete-Cholesky
G	Irradiation (W/m^2)
H	Height (m)
I	Intensity (W/m^2)
I_b	Black body intensity (W/m^2)
k	Thermal conductivity (W/mK)
L	Length of the domain of study (m)
N	Conduction radiation parameter
Nu	Nusselt number
p	Pressure (N/m^2)
Pr	Prandtl number
q	Flux (W/m^2)
$FVDM$	Finite volume discrete ordinate method
Ra	Rayleigh number
T	Temperature (K)
V	Velocity vector (m/s)
W	Window (m)
Greek symbols	
β_T	Thermal expansion coefficient (1/K)
ϵ	Emissivity
κ_a	Absorption coefficient (1/m)
ρ	Density of the fluid (kg/m^3)
τ	Optical thickness
ϕ	Scalar
Subscripts	
$cond$	Conduction
c	Cold wall
co	Collimated beam
$conv$	Convection
f	Face centre
$free$	Free stream
i, j	Tensor indices
nb	Neighbour cell
p	Cell centre
rad	Radiation
t	Total
W	Window
w	Width